Journal of The Electrochemical Society

Complexation of F^- by Li^+ and Mg^{2+} Ions as Inorganic Anion Acceptors in Lactone-Based Li^+/F^- and Mg^{2+}/F^- Hybrid Electrolytes for Fluoride Shuttle Batteries

To cite this article: Mitsuo Kawasaki *et al* 2022 *J. Electrochem. Soc.* **169** 110508

Journal of The Electrochemical Society, 2022 **169** 110508

Complexation of F^- by Li^+ and Mg^{2+} Ions as Inorganic Anion Acceptors in Lactone-Based Li^+/F^- and Mg^{2+}/F^- Hybrid Electrolytes for Fluoride Shuttle Batteries

Mitsuo Kawasaki,[1,z] Ken-ichi Morigaki,[1] Gentaro Kano,[1] Reiji Takekawa,[2] Junichi Kawamura,[2] Yuko Yokoyama,[3] Kenji Kano,[1] Takeshi Abe,[3] and Zempachi Ogumi[1]

[1]*Office of Society-Academia Collaboration for Innovation, Kyoto University, Gokasho, Uji, Kyoto 611-0011, Japan*
[2]*Institute of Multidisciplinary Research for Advanced Materials, Tohoku University, 2-1-1 Katahira, Aoba-ku, Sendai, 980-8577, Japan*
[3]*Graduate School of Engineering, Kyoto University, Katsura, Nishikyo, Kyoto 615-8510, Japan*

The development of high-quality fluoride-ion transporting electrolytes is a crucial demand for fluoride shuttle batteries (FSBs). However, the uncontrolled chemical and electrochemical activities of fluoride ions narrow the available potential window, hindering the development of high-voltage FSB cells. We present a method for upgrading recently developed lactone-based liquid fluoride electrolytes by complexation of F^- with Li^+ and Mg^{2+} ions. In the resultant Li^+/F^- and Mg^{2+}/F^- hybrid electrolytes, Li_2F^+ and MgF^+ were the most probable soluble complexes, and the effective fluoride concentrations could reach ∼0.15 M along with excess $Li^+(Mg^{2+})$ ions. Unique interactions between F^- and $Li^+(Mg^{2+})$ were observed using ^{19}F nuclear magnetic resonance spectroscopy. $Li^+(Mg^{2+})$ ions thus served as inorganic anion acceptors with ultimate redox stabilities to expand the negative potential window of the electrolytes to near −3 V vs SHE. The proposed complex formation was also supported by a conductometric titration method. We demonstrated the superior and versatile electrochemical performances of the Li^+/F^- hybrid electrolyte, which enabled reversible charge/discharge reactions of various metal electrodes and composite electrodes in a wide range of redox series. Further, the Li^+/F^- hybrid electrolyte opened valid new reaction paths for aluminum, making it a promising negative electrode in high-voltage FSB cells.

 [DOI: 10.1149/1945-7111/ac9a05]

Manuscript submitted May 11, 2022; revised manuscript received September 19, 2022. Published November 4, 2022.

Supplementary material for this article is available online

Fluoride shuttle batteries (FSBs) are secondary batteries that rely on the transport of fluoride species between positive and negative electrodes,[1–3] where the reversible half-cell reactions, 1 and 2, proceed with metals, $M^{(I)}$ and $M^{(II)}$, respectively, preferably with as significant a difference as possible between their redox potentials.

$$M^{(I)}F_x + xe^- \rightleftarrows M^{(I)} + xF^- \quad [1]$$

$$M^{(II)} + yF^- \rightleftarrows M^{(II)}F_y + ye^- \quad [2]$$

When both metals, $M^{(I)}$ and $M^{(II)}$, allow for conversion reactions involving multi-electron transfers ($x, y \geqslant 2$), it is possible to achieve a sizeable gravimetric energy density. For example, with Cu as $M^{(I)}$ and Al as $M^{(II)}$ and a full-cell voltage of approximately 2.3 V, the theoretical value exceeds 1000 Wh kg^{-1}. However, electrochemical control over the above reactions is highly challenging, requiring metal/insulator reversible redox conversions via interfacial electron transfers at the respective electrodes. Furthermore, the system must cope with quite the large (∼3 fold) volume changes of the active materials associated with reactions 1 and 2. Finally, the system must have an electrolyte in solid or liquid form that ensures a sufficiently high fluoride-ion flux to sustain the relevant redox reactions at both electrodes under minor interelectrode resistance.

Given these critical issues, high-boiling organic-liquid-based systems are the most promising candidates. They allow for facile room-temperature cell operation under ambient pressure with the high flexibility of the liquid media able to buffer the volume changes of the active materials. A common strategy to fabricate such fluoride-ion transporting liquid electrolytes is to use organic fluoride salts such as alkylammonium or substituted alkylammonium fluorides[4,5] However, they are not ideal for FSBs because the resulting ammonium cations with β-hydrogen are vulnerable to Hoffman elimination,[6] yielding olefines and amines. One might circumvent this problem by choosing organic cations without β-hydrogen, but the resulting fluoride ions may still limit the electrochemical stability of the electrolyte.[3]

Another method with a broader range of material options uses anion acceptors (AAs) with solid affinities for fluoride ions, forming alkali cations and AA-complexed fluoride ions and enabling inorganic alkali fluorides to be soluble even in low-polarity organic solvents. The fundamental roles of organic AAs and the optimum conditions for their use in conjunction with tetraglyme and some other solvents have been argued extensively in the series of reports by Konish and co-workers.[7–9] and by Kucuk and co-workers.[10–14] However, the overall improved half-cell performances, studied primarily for BiF_3 composite electrodes, still showed limits in terms of cyclability and reversibility.

Yamamoto and co-workers reported on the successful operation of a CuF_2 positive electrode, achieving almost full utilization of the CuF_2 active material in a fluorohydrogenated ionic liquid.[15,16] The system featured an unusually high room-temperature ionic conductivity (∼100 mS cm^{-1}) owing to the fluorohydrogenated anions, $(FH)_nF^-$, which were reportedly involved directly in the conversion reactions between CuF_2 and Cu. However, unavoidable reductive hydrogen evolution in this system severely limits the negative potential window for constructing FSBs with high cell voltages.

To further advance the FSB research and development, we recently established a different methodology to tailor lactone-based liquid electrolytes.[17] We used a solvent substitution method, in which CsF or KF was dissociated simply through solvation by gamma-butyrolactone (GBL). Although the maximum fluoride-ion concentration achieved by the technique was ∼0.05 M, the electrolytes behaved as strong electrolytes providing a maximum ionic conductivity of 0.8 mS cm^{-1} and could drive reversible metal/metal-fluoride conversions at room temperature for a wide range of metal electrodes. Nevertheless, the issue of the negative potential window has remained, restricting the negative electrode materials to Zn in the least noble limit of the redox series. We attributed this drawback to the GBL-solvated, virtually free, active

[z]E-mail: m-kawasaki@saci.kyoto-u.ac.jp; mitsuok@ktd.biglobe.ne.jp

fluoride ions, which promoted the reductive decompositions of the solvent.

The present study developed a strategy to upgrade the lactone-based liquid electrolyte to be compatible with a considerably more negative potential regime extending to near or beneath −3 V vs SHE. The underlying principle is the complexation of F^- by Li^+ or Mg^{2+} ions, as follows:

$$F^- + nLi^+ \rightleftarrows Li_nF^{(n-1)+} \quad [3]$$

$$F^- + mMg^{2+} \rightleftarrows Mg_mF^{(2m-1)+} \quad [4]$$

Note that $Li^+(Mg^{2+})$ must be present at sufficiently high concentrations in the electrolyte for the complexes on the right-hand side to be dominant or at least significant. Otherwise, the following precipitation reactions would predominate:

$$F^- + Li^+ \rightleftarrows LiF\downarrow \quad [5]$$

$$2F^- + Mg^{2+} \rightleftarrows MgF_2\downarrow \quad [6]$$

We found that Li^+ is the only alkali cation that forms a soluble complex with F^- in GBL, whereas Ca^{2+} and Ba^{2+} (alkali Earth cations) behaved similarly to Mg^{2+}. The complexation of F^- by Mg^{2+} and Ca^{2+} to produce soluble order one complexes, MgF^+ and CaF^+, has been reported in aqueous solutions.[18–20] The soluble complexes between F^- and alkali-Earth cations in GBL most likely occur in the same order. As for complexation involving Li^+, the order two complex, Li_2F^+, is the most plausible species. The unique complexing capability of Li^+ among the alkali cations may be related to the specific geometrical and electronic structures of Li_2F^+ in polar solvents. We refer to liquid electrolytes containing such complexes as the primary sources of electrochemically active fluoride ions as $Li^+/F^-(Mg^{2+}/F^-)$ hybrid electrolytes. As discussed in this article, the $Li_2F^+(MgF^+)$ complexes in GBL add extra flavors to the electrolyte.

We should also emphasize that the $Li^+(Mg^{2+})$ ions in the hybrid electrolytes serve as inorganic AAs that are hardly reduced or oxidized further, thus assuming ultimate electrochemical stability. However, care should be taken because $Li^+(Mg^{2+})$ ions can hardly dissolve alkali fluorides in GBL, unlike the aforementioned organic AAs. Instead, what we emphasize in this article is another critical role of AAs in controlling the electrochemical activity of F^- ions. $Li_2F^+(MgF^+)$ complexes, as such, help us circumvent reductive solvent decomposition without serious interference with the metal/metal-fluoride redox conversions. We also found that $Li_2F^+(MgF^+)$ complexes and excess $Li^+(Mg^{2+})$ ions together could promote fluoride chemical dissolution, impacting the charge/discharge behaviors in the hybrid electrolytes. Furthermore, the Li^+/F^- hybrid electrolyte activated valid reaction paths for an aluminum-based electrode, making it a promising negative electrode for high-voltage FSB cells.

This paper focused first on the fundamental characterization of $Li^+/F^-(Mg^{2+}/F^-)$ hybrid electrolytes wherein the complexation of F^- by $Li^+(Mg^{2+})$ ions occurred. We then investigated the efficiencies of various plain metal electrodes in the form of plates or foils for reversible fluorination in hybrid electrolytes. The results corroborated the superior performance and capabilities of the Li^+/F^- hybrid electrolyte for application in FSBs.

The Li^+/F^- hybrid electrolyte also enabled highly reversible and high-capacity operations of practical composite electrodes based on Bi/BiF_3 and Cu/CuF_2 redox conversions. Thus, their combinations with the Al-based negative electrode provide prototypes of high-voltage FSBs at the laboratory level. However, the details on these more practical issues will be presented elsewhere in a separate article to save space.

Experimental

Materials.—Cesium fluoride (CsF, 99.99%) and bismuth fluoride (BiF_3, 99.9%) powders were purchased from Kojundo Chemical Lab. Co., Ltd. γ-Butyrolactone (GBL, 99.5%), N-methyl pyrrolidone (NMP, 99.5%), lithium bis(fluorosulfonyl)imide (LiFSI, 99%), and magnesium bis (trifluoromethane sulfonyl)imide ($Mg(TFSI)_2$) of lithium-ion-battery grade were obtained from Kishida Chemical Co. Ltd. Copper fluoride (CuF_2, 98%) and ferrocene ($(C_5H_5)_2Fe$, 98%) powders were sourced from Sigma-Aldrich. Acetylene black (AB, non-press) was obtained from DENKA; activated carbon (ACC) powders with a particle size of ∼20 μm (CAT. No. 01085–02, CAS RN 7440-44-0) from Kanto Chemical Co., Ltd.; polyvinylidenedifluoride (PVDF) solution (5 wt% KF polymer/NMP solution, L#9305) from KUREHA; and polytetrafluoroethylene (PTFE) resins (Fine Powder, #6 J) from Chemours-Mitsui Fluoroproducts Co., Ltd. Al foil (20 μm thick) for use as a current collector was purchased from Hohsen Corporation, and an Al-laminated film (100 μm-thick) was obtained from Dai Nippon Printing Co., Ltd. A nickel sponge was from Sumitomo Electric Industries, Ltd. Other high-purity metals (in plates, foils, meshes, or wires) were received from Nilaco Corporation. All other common chemicals were of special reagent grade and obtained from Fujifilm Wako Pure Chemical Corporation or Kanto Chemical Co., Ltd. Ultrapure water for use in the relevant aqueous solutions was prepared using a Direct-QUV3 water purification system (Merck KGaA).

Preparation and chemical analyses of liquid electrolytes.—The as-received GBL solvent had a water content of 30 ppm or less, as checked by the Karl Fischer titration method (Hiranuma, AQ-2200). 1 M(2 M) GBL solutions of $LiFSI(Mg(TFSI)_2)$, keeping the low level of water, were prepared by dissolving the respective salts of battery grades at room temperature. The GBL-based, plain, fluoride-ion electrolyte (CsF/GBL) was prepared according to the solvent-substitution method developed in the previous work, requiring mixing aqueous CsF solution (1.4 M) with GBL in a 1 to 10 volume ratio.[17] Despite a large amount of water in the initial mixture, the primary stage of high-temperature (∼130 °C) water vaporization under stirring for about 1.5 h, followed by an Ar-bubbling-assisted continued dehydration for 0.5 to 1 h, could remove the water from CsF/GBL to a level well below 50 ppm.

The resultant CsF/GBL electrolyte was combined with the 1 M (2 M) GBL solutions of LiFSI ($Mg(TFSI)_2$) to fabricate a series of $Li^+/F^-(Mg^{2+}/F^-)$ hybrid electrolytes. The detailed procedure will be described in subsequent sections.

The compositions of the respective electrolytes were verified by quantifying the Cs^+, Li^+, and Mg^{2+} ions using inductively coupled plasma-mass spectrometry (ICP-MS, Agilent 7700). Complementary semi-quantitative information regarding the effective content of F^- ions was obtained by using a simplified water analysis tool (PACKTEST from Kyoritsu Chemical-Check Lab, Corp.). The ionic conductivity was measured by AC impedance spectroscopy at 0 V. Analysis was performed in the frequency range of 1 MHz to 10 Hz with an amplitude of 50 mV.

The ^1H,^{19}F, ^{13}C, ^7Li, ^{25}Mg, and ^{133}Cs nuclear magnetic resonance (NMR) spectra were acquired using a Bruker Avance III (11.7 T) spectrometer equipped with a BBFO broadband probe. In addition, we used Bruker Avance III (14.1 T) spectrometer equipped with a TCI cryoprobe for the ^{19}F NMR spectroscopy to gain more precise signals above the broad background continuum. The chemical shifts were determined by referencing the following external standard materials; TMS (0 ppm for ^1H and ^{13}C), fluorobenzene (−113.15 ppm for ^{19}F), and 0.1 M aqueous $CsNO_3$ solution (0 ppm for ^{133}Cs).

Cell setup and electrochemical measurements.—Electrochemical measurements, including cyclic voltammetry (CV) and galvanostatic charge/discharge cycle tests, were performed with a series of potentiostats (BioLogic SP-200, SP-240, and SP-300) using a three-electrode conical beaker cell (EC Frontier Co., Ltd., VB7 cell kit)[17] or a three-electrode Al-laminated cell that was assembled and vacuum-sealed inside a dry room.[21] In the half-cell mode, the cells consisted of a working electrode made of the metal or metal-fluoride composite of interest, a counter electrode made of either nickel sponge or an activated-carbon-based composite sheet,[21] a silver wire reference electrode, and the given liquid electrolyte of 0.4–0.8 ml (for the beaker cell) or 1.5 ml (for the laminated cell).

The reference Ag electrode potential in the lactone-based electrolytes was scaled to 0.35 V vs SHE, based on calibration using ferrocene as the internal standard.[22] The effective contact area of the working electrode with the liquid electrolyte was set to 10 to 40 mm^2. The surrounding area was masked with a sealant film to block contact with the liquid whenever necessary. For the beaker cell, the entire cell assembly during the electrochemical measurements was placed in a low-pressure vacuum chamber with a continuous dry Ar gas flow to maintain a steady-state Ar pressure of 10 kPa. The corresponding atmosphere inside the vacuum chamber was confirmed to compare favorably with that in an Ar-filled glove box according to residual gas analysis with a quadrupole mass spectrometer (PrismaPro, Pfeiffer Vacuum).

Structural and chemical analyses of active materials.—The crystal structures of the active materials and their changes during the charge/discharge processes were examined by *ex-situ* X-ray diffraction (XRD) measurements using Cu K_α radiation (8.04 keV; Rigaku, SmartLab) with an airtight specimen holder (Bruker, A100-B36) designed for environmentally sensitive materials. After charging or discharging, the sample was removed from the electrolyte to an Ar-filled glove box, washed with GBL, dried under vacuum, mounted on the sample supporting table of the specimen holder, and then tightly shielded from the air by a domed plastic cap. The surface morphologies and elemental distributions on the electrode surface due to charging and discharging were inspected by field emission scanning electron microscopy (FE-SEM) and energy-dispersive X-ray spectroscopy (EDX) using Hitachi SU6600 or SU8200 instrument. X-ray photoelectron spectroscopy (XPS) depth-profiling data were obtained using a PHI Quantera SXM instrument (Ulvac-Phi, Inc.). An airtight vessel was used to transfer samples from the Ar-filled glove box to the XPS analysis chamber.

Results and Discussion

Characterization of hybrid electrolytes.—We prepared a series of hybrid electrolytes with relatively low fluoride concentrations by mixing the recently developed lactone-based fluoride-ion electrolyte[17] (CsF/GBL, containing 50 mM of F^- ions) with 2 M LiFSI/GBL or 1 M $Mg(TFSI)_2$/GBL in various volume ratios. It is also possible to choose other GBL-soluble lithium and magnesium salts unless the corresponding anions form insoluble salts such as $Li_2F(BF_4)$.[23]

Figure 1 shows a collection of photo images of the $Li^+/F^-(Mg^{2+}/F^-)$ mixtures. In the case of the Mg^{2+}/F^- series (Fig. 1a), the hybrid states (transparent solutions) and those causing immediate precipitation of MgF_2 (colloidal suspensions) were demarcated by a critical Mg^{2+}/F^- molar mixing ratio of 1:1. This ratio suggests that the order one complex, MgF^+, is the most likely dominant form of GBL-soluble Mg^{2+}/F^- complexes. We observed similar behaviors for Ca^{2+}/F^- and Ba^{2+}/F^- hybrid states.

In contrast, the Li^+/F^- mixtures (Fig. 1b) displayed a gradual transition from transparent to colloidal state, and a faint colloidal clouding was already noticeable at a Li^+/F^- molar ratio of around 7:1. Then, almost complete fluoride-ion precipitation seemed to occur at Li^+/F^- molar ratios near 2:1 (the rightmost image of Fig. 1b). These behaviors suggest that a higher-order (probably order two) complex, Li_2F^+, is the most likely form in equilibrium with Li^+ and F^- (reaction 3). Notably, neither Na^+ nor K^+ produced soluble complexes with F^- ions, and the corresponding mixtures turned into colloidal suspensions irrespective of the mixing ratios. The reason for the unique behavior of Li^+ compared to other alkali cations is discussed in a later section.

Enhanced solubility of fluorides by Li_2F^+ and MgF^+.—The equilibrium constants for the common precipitation reactions, 5 and 6, are given by the solubility products, $K_{1,sp}$, defined by $[F^-][Li^+]$ and $[F^-]^2[Mg^{2+}]$, respectively, where we approximated the activities of the respective ions by their molarities. Let K_2 represent the equilibrium (complex formation) constant for reactions 3 and 4, where we now assume that $n = 2$ ($m = 1$). Combining reactions 3 through 6, we derive the following equilibrium reactions:

$$LiF\downarrow + Li^+ \rightleftarrows Li_2F^+ \quad [7]$$

$$MgF_2\downarrow + Mg^{2+} \rightleftarrows 2MgF^+ \quad [8]$$

The equilibrium constants (K_d) for reactions 7 and 8 are equal to $K_2 \cdot K_{1,sp}$ and $K_2^2 \cdot K_{1,sp}$, respectively. In practice, even if excess $Li^+(Mg^{2+})$ ions are present, $LiF\downarrow(MgF_2\downarrow)$ does not as easily dissolve as one might expect from reactions 7 and 8, owing to kinetic constraints. However, when $Li_2F^+(MgF^+)$ complexes coexist with the excess $Li^+(Mg^{2+})$ ions, as in the case of the hybrid electrolytes, the situation changes in the behavior of nascent-stage $LiF\downarrow(MgF_2\downarrow)$ precipitates. Namely, the $Li_2F^+(MgF^+)$ complexes likely act as self-catalysts for the dissolution of $LiF\downarrow(MgF_2\downarrow)$, presumably according to the following schemes:

$$LiF\downarrow + Li^+ + [Li_2F^+] \rightarrow 2Li^+ + [Li_2F_2] \rightarrow Li_2F^+ + [Li_2F^+] \quad [9]$$

$$MgF_2\downarrow + Mg^{2+} + [2MgF^+] \rightarrow 2Mg^{2+} + [2MgF_2] \rightarrow 2MgF^+ + [2MgF^+] \quad [10]$$

Here, the species in parenthesis represent self-catalysts and hypothetical neutral intermediates based on the assumption of F^- abstraction from $LiF\downarrow(MgF_2\downarrow)$ by $Li_2F^+(MgF^+)$. One of the experimental supports for reactions 9 and 10 is the observation that we could readily redissolve a noticeable colloidal clouding in the $Li^+/F^-(Mg^{2+}/F^-)$ hybrid electrolytes by adding a small amount of extra $Li^+(Mg^{2+})$ ions. The conductometric titration experiments also supported the proposed catalytic function of $Li_2F^+(MgF^+)$ (see subsequent sections and Supplementary Material, Section S1). Furthermore, we have established a valuable procedure that takes advantage of reactions 9 and 10. It allowed us to prepare hybrid electrolytes with much higher concentrations (typically 0.15 M) of $Li_2F^+(MgF^+)$ than those achieved in the simple mixtures illustrated in Fig. 1 (limited to ~38 mM).

The method starts with a mixture (1:13.3 volume ratio) of 1.5 M aqueous CsF solution and a hybrid electrolyte constituting 1(0.5) M Li^+ (Mg^{2+}) and 25 mM F^- ions in GBL, followed by high-temperature (⩽150 °C) heating under continuous stirring and Ar gas bubbling long enough to remove residual water to a level of ~30 ppm or less. Since the initial mixture already contained a significant amount of $Li_2F^+(MgF^+)$ complexes together with excess $Li^+(Mg^{2+})$ ions, even when $LiF\downarrow(MgF_2\downarrow)$ occurred in mid-course, reactions 9 and 10 redissolved them preventing growth to bulk solids. We removed unsolvable precipitates remaining in the final solution by centrifugation. The increased concentration of the fluoride species up to ~0.15 M was verified by the absolute Cs^+ (the original counter cation of F^-) concentration measured by the ICP-MS method, the semi-quantitative detection of F^- ions with the simplified water analysis tool, and the ^{19}F NMR spectra taken for the series of Mg^{2+}/F^- hybrid electrolytes (see below). We will refer to this type of hybrid electrolyte as the concentrated version in each series.

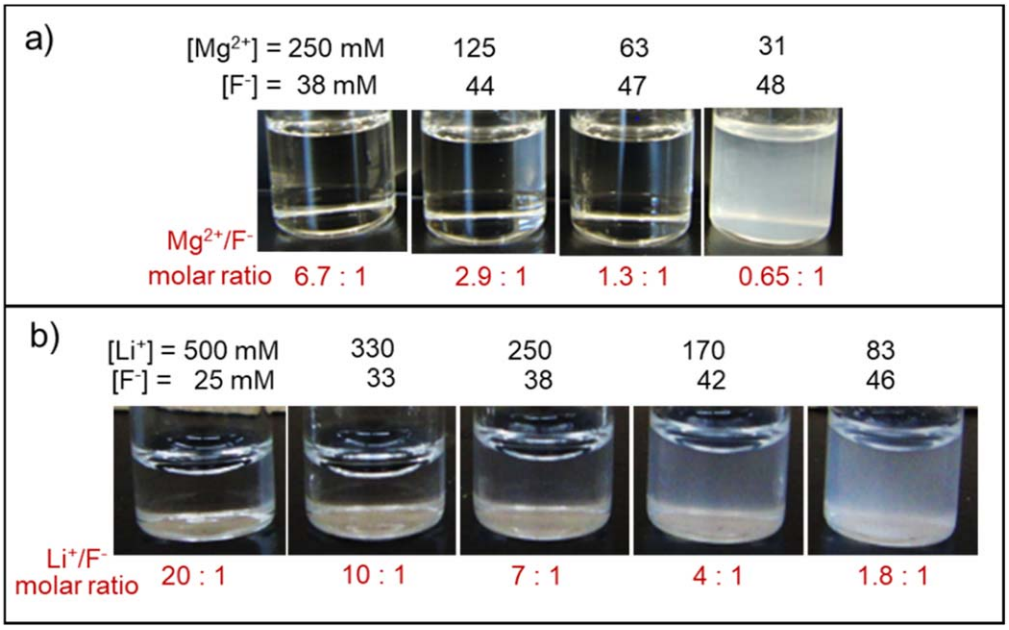

Figure 1. Series of photo-images of the solutions and colloidal suspensions prepared by mixing the CsF/GBL fluoride-ion electrolyte with (a) 1 M $Mg(TFSI)_2$/GBL and (b) 2 M LiFSI/GBL solution in various volume ratios. The effective initial concentrations of Mg^{2+}, Li^+, and F^- before the complex formation are above each image, and the corresponding Mg^{2+}/F^- and Li^+/F^- mixing molar ratios are below each photo.

Notably, the proposed catalytic functions of $Li_2F^+(MgF^+)$ may also promote the dissolution of other fluorides that serve as active materials for FSBs. For example, Fig. 2 shows the measured molar solubilities of commercial metal-fluoride powders stirred in three different GBL-based electrolytes for more than 80 h at room temperature. While the electrolytes composed of only CsF (50 mM) or LiFSI (1 M) caused the minor dissolution of these salts, the Li^+(0.5 M)/F^-(38 mM) hybrid electrolyte resulted in significant solubilities exceeding 15 mM for CuF_2 and PbF_2. MgF^+ complexes had a less pronounced but qualitatively similar effect on promoting fluoride dissolution.

NMR studies of Li_2F^+ and MgF^+ complexes.—NMR is the most powerful tool to investigate the interactions between F^- and $Li^+(Mg^{2+})$ in forming soluble $Li_2F^+(MgF^+)$ complexes in GBL. We acquired a series of ^{19}F spectra for the various states at room temperature.

MgF^+ complexes.—The ^{19}F spectra indicated strong and unique interactions between F^- and Mg^{2+}. Figure 3a shows the typical spectrum of a CsF/GBL electrolyte without MgF^+ complexes. The sharp peak at −137 ppm accounted for 80% of the total integrated signal intensity and likely reflected the lowest-energy solvation of F^- by GBL. The four minor peaks on the right-hand side suggested that other forms of solvation were present to a limited extent. We may have further insight into the F^-–solvent interactions by carefully analyzing the minor peaks in the ^1H and ^{13}C spectra, but the presently available data are not sufficient to draw a conclusive picture regarding such fine details of the solvation structure for F^- in GBL. Note, in addition, that none of the ^{19}F peaks observed for the lactone-based electrolytes seem to have arisen from the problematic FHF^- ions because both ^{19}F doublet (−155.4 ppm) and ^1H triplet (16.6 ppm), known as the NMR fingerprints of FHF^-,[24] were absent irrespective of the composition of the electrolyte.

In Fig. 3b, drastic changes occurred in the ^{19}F NMR spectra of the Mg^{2+}/F^- hybrid series. The sharp signals in the –130 to –150 ppm region disappeared, and there showed up much broader ^{19}F signals with some fine structures, shifting toward more negative chemical shifts. The $TFSI^-$ anion gave a far-off ^{19}F peak at approximately –79.4 ppm. The chemical shifts of around –180 ppm are close to that reported for solid MgF_2 (–200 ppm).[25] The integrated signal intensities of these broad ^{19}F signals may lack preciseness because of the considerable arbitrariness in background subtraction. However, the approximate peak areas were comparable to 70%–80% of those expected for the F^- ions contained in each electrolyte before complexation by Mg^{2+}. Furthermore, the overwhelmingly strong (but likewise broad) ^{19}F signal obtained for the concentrated version in the series supports the unique method for its preparation based on reactions 9 and 10.

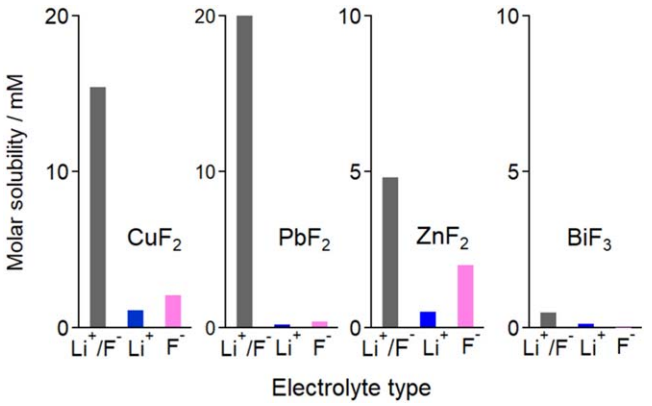

Figure 2. Room-temperature molar solubilities of commercial CuF_2, PbF_2, ZnF_2, and BiF_3 powders in three different types of GBL-based electrolytes; (Li^+/F^-) consists of 0.5 M LiFSI and 38 mM CsF; (Li^+) 1 M LiFSI, and (F^-) 50 mM CsF.

The above results suggest that equilibrium reaction 4 strongly favors the complex state where Mg^{2+} affects the chemical shift and substantially broadens the peak width in the ^{19}F NMR signal. The latter seemingly contradicts the conception that NMR signals from molecular or ionic species in liquids should instead be sharpened by the exchange-narrowing due to fast molecular motion. The observed anomaly suggests that the MgF^+ complex, together with proximal solvent molecules and/or $TFSI^-$ anions, may form manifold structures with a wide configurational parameter space, thereby causing chemical exchange broadening. However, this issue requires further

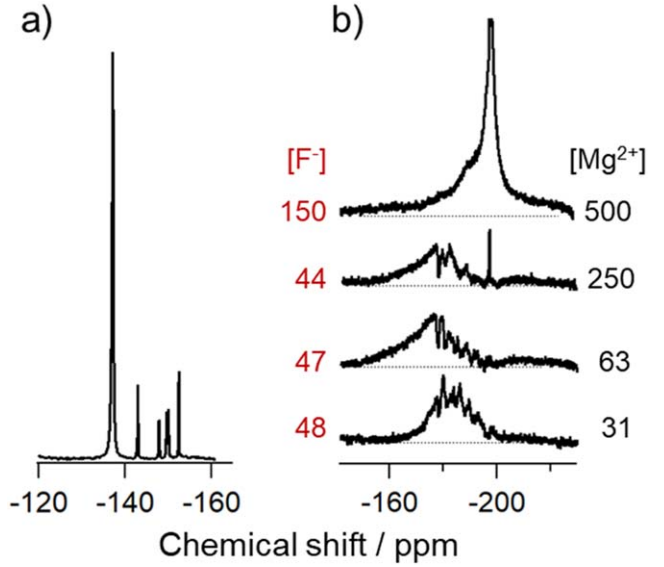

Figure 3. Background subtracted ^{19}F NMR spectra taken of (a) 50 mM CsF/GBL fluoride-ion electrolyte and (b) a series of Mg^{2+}/F^- hybrid electrolytes; the concentrated version (top) and three kinds of standard mixtures with varied Mg^{2+}/F^- molar ratios.

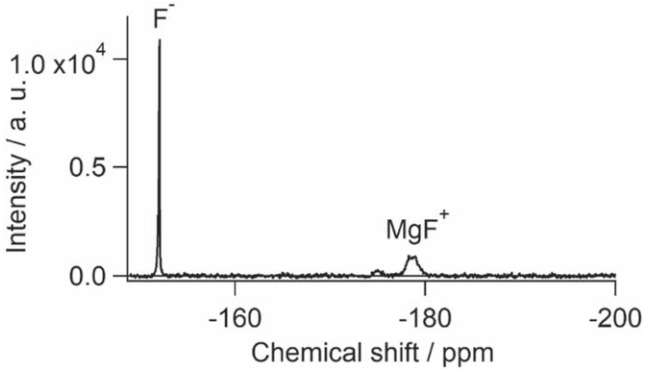

Figure 4. A background-subtracted ^{19}F NMR spectrum taken for the supernatant liquid prepared from the Mg^{2+}(31 mM)/F^-(48 mM) mixture where the major fraction of F^- precipitated as $MgF_2\downarrow$.

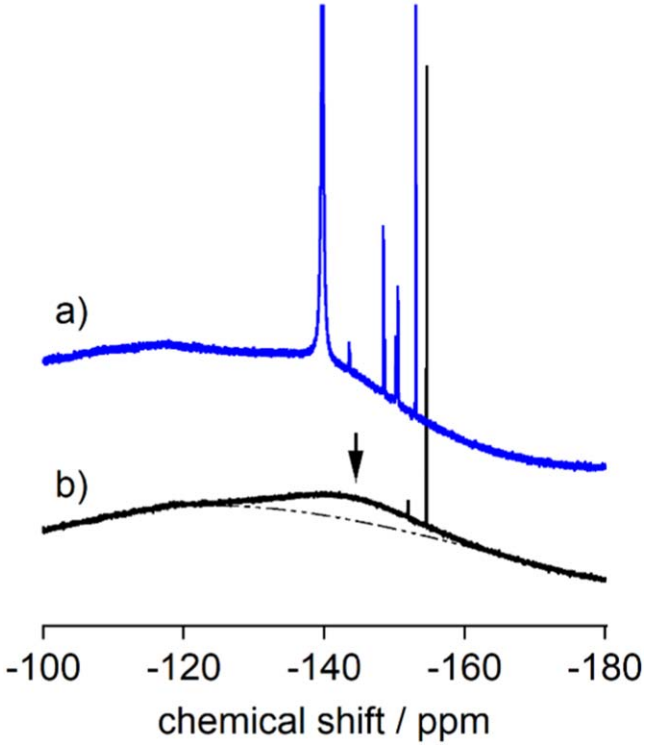

Figure 5. Comparison of ^{19}F NMR spectra between (a) 50 mM CsF/GBL fluoride-ion electrolyte and (b) Li^+/F^- hybrid electrolyte with $[Li^+] = 500$ mM and $[F^-] = 38$ mM. The arrow points to a potential broad signal difficult to distinguish from the background continuum.

experimental and theoretical studies. Note that the MgF^+ complexes must still act as the sole source of fluoride ions for metal/metal-fluoride conversion in the Mg^{2+}/F^- hybrid electrolytes (see below).

We also obtained valuable information about the MgF^+ complex formation from the ^{19}F NMR spectra of Mg^{2+}/F^- mixtures in which the precipitation of $MgF_2\downarrow$ overwhelmed the complex formation. The colloidal suspension shown on the far right of Fig. 1a is a typical example. We settled the whitish precipitates by centrifugation and obtained the ^{19}F NMR spectra (Fig. 4) for the supernatant liquid. Figure 4 revealed that not all the F^- ions precipitated as $MgF_2\downarrow$, but a noticeable fraction survived as either F^- (sharp residual peak at –152 ppm) or MgF^+ (broad signal at –180 ppm). The integrated peak intensities of these signals suggested that they were present in the supernatant liquid at estimated concentrations of 2.3 mM and 2.0 mM, respectively. The results indicate that 91% of the initially mixed F^- ions precipitated as $MgF_2\downarrow$, suggesting that uncomplexed Mg^{2+} ions remained at 7.1 mM. These values allow for a crude estimate of the equilibrium constants, $K_{1,sp}$ and K_2, giving 3.8×10^{-8} and 120, respectively. The latter supports the prediction from Fig. 1a of a significantly large complexing constant for the formation of MgF^+. Equivalently, we can evaluate the solubility product; $K_{3,sp} = [MgF^+][F^-]$, for the following equilibrium reaction:

$$MgF^+ + F^- \rightleftarrows MgF_2\downarrow \qquad [11]$$

$K_{3,sp}$ is equal to the product of $K_{1,sp}$ and K_2, i.e., 4.7×10^{-6}. This value agreed reasonably with 5×10^{-6}, obtained independently by conductometric titration (see below).

Li_2F^+ complexes.—The Li^+/F^- hybrid electrolytes must contain some molecular fluoride species at the same concentration as the Cs^+ cations determined by ICP-MS. We also confirmed the presence of a significant amount of fluoride-ion sources through semi-quantitative colorimetry using the simple water analysis tool. The capability of Li^+/F^- hybrid electrolytes to drive the redox conversion from metal to metal fluoride is likely dependent on such fluoride species.

Figure 5 compares the ^{19}F spectrum of the original CsF/GBL electrolyte that exhibited a series of sharp peaks with that obtained for a Li^+/F^- hybrid electrolyte with initial Li^+ and F^- before their complexation, 500 mM and 38 mM, respectively. A sharp but minor peak observed for the Li^+/F^- hybrid electrolyte at –154 ppm is likely due to uncomplexed fluoride ions at the estimated (from its peak area) concentration of 2.2 mM. However, we could not find any other fluoride signals, including those assignable to Li_2F^+ complexes, except for a broad signal (Fig. 5b) that was difficult to distinguish from the background. The apparent lack of ^{19}F peaks associable with Li_2F^+ complexes points to some different effects of the complexation of F^- by Li^+ ions. This effect may also be relevant to the unique complexing ability for F^- exhibited by Li^+, different from the other alkali cations. Given that Li_2F^+ is the most probable form of the Li^+/F^- complexes, it would be worth considering the most stable geometrical and electronic structures of Li^2F^+ in the hybrid electrolyte.

According to the currently available experimental and theoretical thermochemical data,[26–28] Li_2F^+ is stable in the gas phase, and the formation of Li_2F^+ from $2Li^+$ and F^- is largely exothermic by ~9

eV.[27] On the other hand, we expect Li^+ and F^- to be stabilized by ~4 eV by solvation in polar solvents like water and GBL. It may be large enough to offset the binding energy of Li_2F^+ relative to $2Li^+$ plus F^- in liquid unless Li_2F^+ benefits from solvation energy that is at least comparable to those of Li^+ and F^-. This condition may not be the case if Li_2F^+ adopts the extended linear molecular structure present in the gas phase, as this may have a considerably larger effective ionic radius for solvation than that of Li^+. Notably, a neural Li_2F favors a bent C_{2v} symmetry structure where an extra electron occupies the 2σ molecular orbital (MO), which is bonding through a Li–Li interaction.[29] The bending shortens the Li–Li distance, thus increasing the Li atomic orbital (AO) overlap. We speculate that Li_2F^+ favors a similar bent form in GBL, leaving a vacant 2σ MO but acquiring a small effective ionic radius, increasing the solvation energy accordingly. This hypothetical structure unique to Li_2F^+ might also account for the failure of the complexation of F^- by Na^+ and K^+.

However, the question of the missing ^{19}F NMR peaks for the Li_2F^+ complexes remains. What seems relevant is the probably more labile nature of Li_2F^+ than MgF^+, as reflected in the less well-defined critical Li^+/F^- ratio demarcating the complex formation and LiF↓ precipitation regimes (cf. Fig. 1b). The looser complexation of F^- by Li^+ connotes a more facile de-complexation of Li_2F^+ and a more expansive coordination parameter space for the complex state than for MgF^+. Given that the dynamic changes among these states occur on microsecond to millisecond timescales, they potentially broaden the NMR spectral lines to the extent that we no longer observe distinguishable peaks.

Notably, despite the essential question discussed above, Fig. 5 serves as the only presently available experimental base on which we may address the plausible thermodynamic parameters for the complex formation in the Li^+/F^- hybrid electrolyte. One necessary assumption is that the balance after deducing the 2.2 mM (yielding the minor ^{19}F peak in Fig. 5b) from the total fluoride concentration (38 mM) was solely due to the Li_2F^+ complexes. It then follows that uncomplexed Li^+ ions remained at 430 mM. These numbers immediately allow for crude estimates of $K_{1,sp}$, K_2, and $K_{3,sp}$ ($[Li_2F^+][F^-]$) as 9.5×10^{-4}, 90, and 8.1×10^{-5}, respectively. Note that $K_{3,sp}$, in this case, is equal to $K_{1,sp}{}^2K_2$. These values seem to be consistent with the proposed looser complex structure of Li_2F^+ as compared to MgF^+.

Conductometric titration of F^- by $Mg^{2+}(Li^+)$ and $Mg^{2+}(Li^+)$ by F^-.—We performed a series of independent conductometric titration measurements to gain quantitative information for the $MgF^+(Li_2F^+)$ complex formation and relevant thermodynamic parameters. The results are described in detail in Supplementary Material, Section S1. In short, when we titrate arbitrary electrolytes with F^- ions with $Mg^{2+}(Li^+)$ and vice versa, the precipitation and complex formation change the ionic conductivity of the liquid in a manner that is different from that in the absence of such interactions. Careful analysis of the resultant titration curves for the Mg^{2+}/F^- hybrid electrolyte led us to estimate the solubility product, $K_{3,sp} = [MgF^+][F^-]$, as $\sim 5 \times 10^{-6}$. This value reasonably agreed with 4.7×10^{-6}, as calculated based on the ^{19}F NMR spectrum shown in Fig. 4.

Electrochemical performance of hybrid electrolytes.— *CV characteristics of plain metal electrodes.*—The actual performance of hybrid electrolytes toward FSBs can be evaluated preliminarily by the reactions of various plain metal electrodes of interest. Anodic

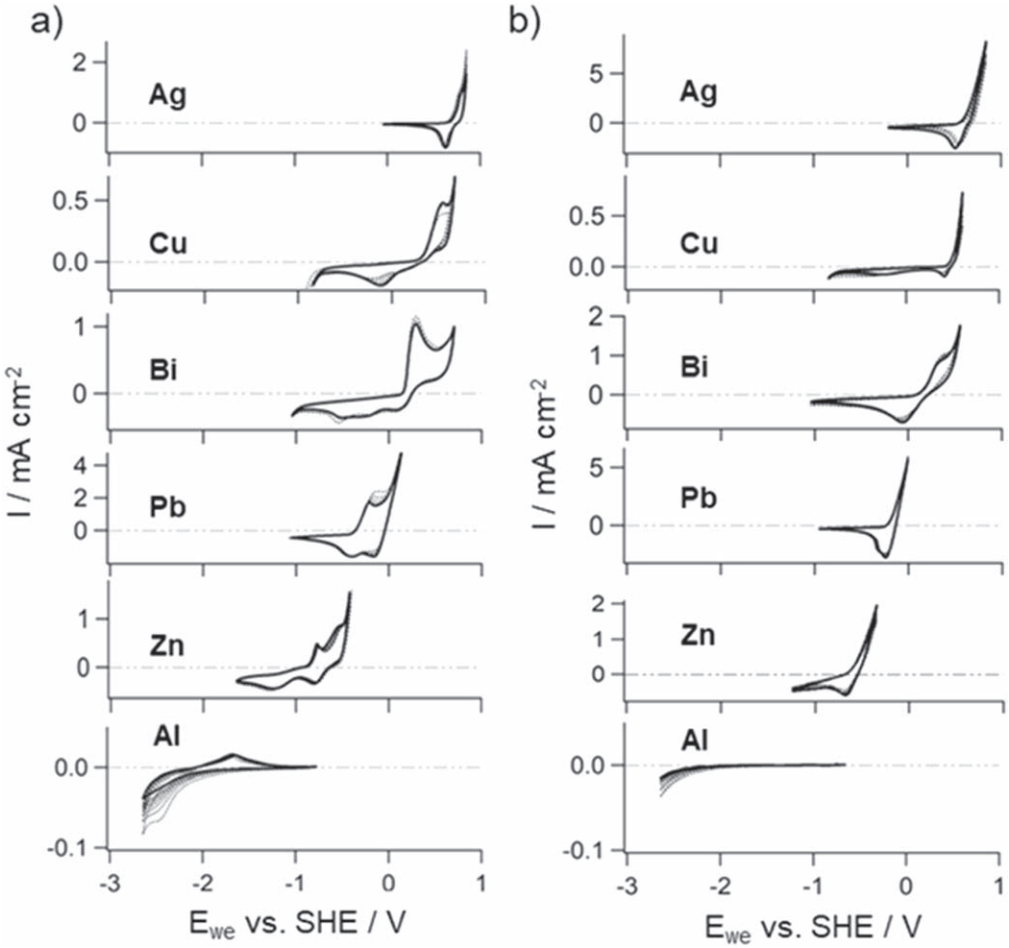

Figure 6. Series of CV curves (at 10 mV/s scan rate) measured for various mechanically polished metal electrodes in (a) Li^+/F^- and (b) Mg^{2+}/F^- hybrid electrolytes with a standard concentration of F^-, 38 mM, before complexation by Li^+ and Mg^{2+}.

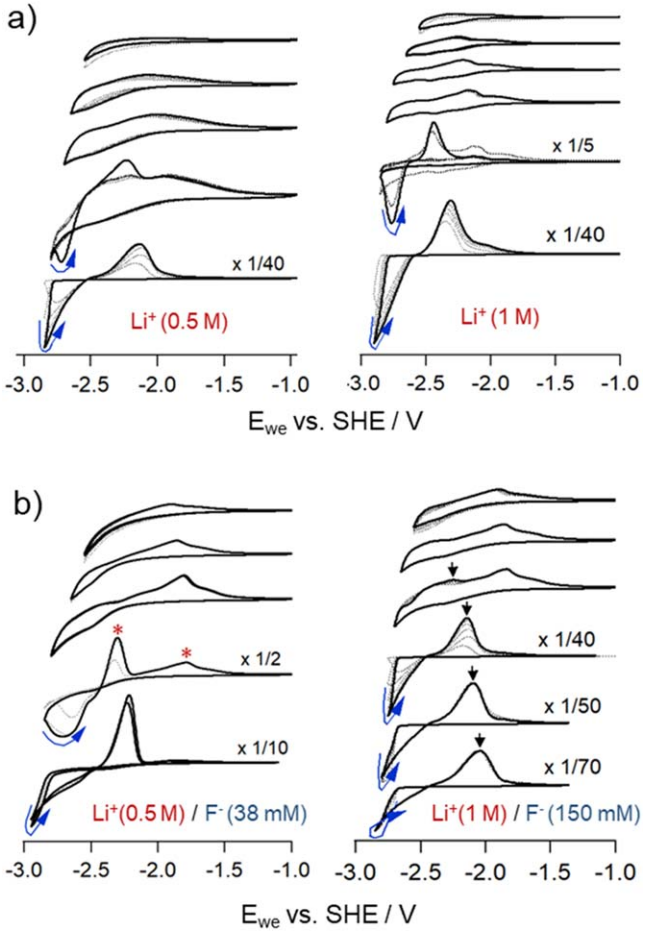

Figure 7. Series of CV curves (at 10 mV s^{-1}) measured for polished Al foils with the switching potential of the cathodic sweep systematically lowered (from top to bottom) to increase the maximum cathodic polarization. (a) Responses in the reference electrolytes made of LiFSI salts alone with the Li^+ ion concentrations of 0.5 M (left) and 1 M (right). The curved blue arrows indicate strong hysteresis in the large cathodic current caused by a massive lithiation. (b) Comparative responses in the standard (left) and concentrated (right) versions of the Li^+/F^- hybrid electrolyte.

metal fluorination produces a fluoride shell on the metal surface. The electronic and ionic properties of the fluoride shell determine how thick it can grow further and how it will affect the subsequent redox reactions. Our previous study using the CsF/GBL electrolyte showed that the fluoride shell thickness varied from tens of nm for Cu to more than hundreds of nm for Pb; however, every fluoride shell passivated the metal surface against anodic metal dissolution under high anodic polarization.[17] Furthermore, the fluoride shells grown sufficiently thick for XRD analysis proved to be in good crystalline states. However, this was not the case for the present hybrid electrolyte systems.

Figure 6 shows a series of CV curves measured for various metal electrodes in Li^+/F^- (Fig. 6a) and Mg^{2+}/F^- (Fig. 6b) hybrid electrolytes. Here, the electrolytes had a composition of 38 mM F^- before complexation with $Li^+(Mg^{2+})$. This small molarity of F^- might arouse questions about how it can be practical for battery applications. However, as shown below, this low fluoride concentration, together with the coexisting 0.5 M(0.25 M) $Li^+(Mg^{2+})$, allowed for observation of the expected stable redox reactions characteristic of the hybrid electrolytes at significant rates for plain metal electrodes (foil or plate). In other cases, such as those involving more practical composite electrodes, the much higher fluoride concentration of 0.15 M, achieved in the concentrated versions of the electrolytes, was preferable. The practical impact of the effective fluoride concentration in the hybrid electrolytes and prospects for future direction will be addressed shortly at the end of Results and Discussion.

The CVs of the Al electrodes in Fig. 6 testify to the successful expansion of the negative potential window edge to near –3 V vs SHE and are also of particular interest for high-voltage FSB applications. The CVs of the Ag electrode, which was the noblest metal examined in Fig. 6, exhibited a distinct anodic signal characteristic of Ag at near 1 V vs SHE. We also confirmed separately that Au and Pt electrodes, much nobler than Ag, gave a significant anodic current that began to rise in the potential region more positive than 1.5 V vs SHE, due probably to the anodic breakdown of the electrolyte. These observations support that the present hybrid electrolytes also allowed for a wide potential window on the positive side.

In Fig. 6a, the CV scan was initiated in the anodic direction for every electrode except Al. The CVs of the Ag through Zn electrodes invariably exhibited distinct anodic peaks or shoulders, along with broad cathodic features in the reverse scan. Such signals were absent in the corresponding CVs measured in a reference electrolyte comprising only LiFSI,[17] which exhibited a large monotonically increasing current due to direct anodic metal dissolution followed by a minor cathodic peak in the reverse scan. Therefore, we attributed the CVs in Fig. 6a to reversible metal fluorination and defluorination, characteristic of the Li^+/F^- hybrid electrolyte. The fluorinated metal surface (i.e., the fluoride shell) should have restrained the anodic metal dissolution. However, in the present case, the resultant metal-surface passivation seemed not very strong because the sharp rises in the anodic current beginning soon after the anodic peak or shoulder most likely represent anodic metal dissolution. In Fig. 6, we restricted the maximum anodic polarization to cut off this irreversible current before it grew too large.

The relatively poor passivation of the fluorinated metal surface in the present case may be explained by assuming that thin fluoride shells are subject to more facile chemical dissolution in the Li^+/F^- hybrid electrolyte than bulk fluoride powders, thereby exposing unprotected metal surfaces and promoting the anodic dissolution under stronger anodic polarization. Although there is no sure evidence for the identification of the narrow anodic wave, this interpretation also seemed consistent with the CV of the Bi electrode exhibiting the most distinct anodic peak in Fig. 6a; note that the corresponding fluoride shell should be the least soluble among the fluoride series (cf. Fig. 2).

Given that the anodic peaks or shoulders in Fig. 6a (except that for Al) are accompanied by the concurrent chemical dissolution of the fluoride shells, the distinguishable cathodic waves in the reverse scan suggest that most of the chemically dissolved fluoride species remained in the vicinity of the working electrode at least in the time scale of the CV scan and contributed to the reversible transformation back to the metallic states. This relationship is supported further by the considerably high Coulombic efficiencies for the cathodic waves under the minor influence of the anodic metal dissolution. The calculated efficiencies for the series of CVs presented in Fig. 6a were approximately 85% (Pb), 90% (Ag and Cu), 95% (Bi), and 100% (Zn). The critical roles of the fluoride chemical dissolution will be discussed further in a subsequent section based on prolonged charge/discharge cycling results. The control over fluoride chemical dissolution is indeed key to tailoring the charge/discharge behaviors of various (particularly positive) electrodes in the hybrid electrolytes.

As for the Mg^{2+}/F^- hybrid system (Fig. 6b), the anodic waves mostly lacked apparent peaks, but some curves (those for Bi and Zn) still exhibited noticeable shoulders attributable to fluorination. The significant cathodic signals in the reverse scan, for which the calculated Coulombic efficiencies likewise reached or exceeded 90% except for Ag, suggest the involvement of a reversible fluorination process similar to that in the Li^+/F^- hybrid electrolyte. As discussed above, the MgF^+ complex state is likely more stable and inert than Li_2F^+, which, in turn, implies that MgF^+ is less

efficient in affording chemically active fluoride ions for metal fluorination. Thus, the corresponding fluoride shell can be more defective or soluble and may serve as a poorer passivation layer.

The behavior of the Al electrode.—The CV responses of the Al electrodes in Fig. 6 are qualitatively unique and must be considered from a different perspective. Aluminum has a redox potential that is so significantly negative that it has not yet been possible to incorporate it into any cells using conventional liquid fluoride electrolytes. The intrinsically poor reactivity of Al arises from the difficulty of the three-electron-transfer reactions between Al and AlF_3, the latter being a strongly insulating material with an extremely large bandgap. In addition, unlike other metal fluorides in the positive redox series, AlF_3 is barely soluble in liquid electrolytes.

Nevertheless, Fig. 6a shows that the Li^+/F^- hybrid electrolyte produced a unique CV with an anodic peak at around −1.7 V vs SHE. Whereas the Mg^{2+}/F^- hybrid electrolyte (Fig. 6b) did not elicit any noteworthy responses in the same potential region. The results point to the activity of the Li_2F^+ complexes or the excess Li^+ ions themselves, altering the otherwise electrochemically inert Al. An obvious explanation is the well-known electrochemical lithiation of Al to $AlLi_x$ alloys.[30–33] We, therefore, compared the series of CVs measured in the Li^+/F^- hybrid electrolytes and reference electrolytes with equivalent concentrations of Li^+ ions but containing only LiFSI; see Fig. 7.

In Fig. 7, we lowered the switching potential (E_{sw}) step-wisely, where the cathodic sweep turned back to allow for increasingly stronger cathodic polarization favoring lithiation. The CVs obtained in the reference electrolytes (Fig. 7a) began manifesting a noticeable reversible wave when E_{sw} was set more negative than −2.6 V vs SHE. This wave probably represents an underpotential deposition of Li onto Al (i.e., partial lithiation in a thin subsurface layer of the Al electrode) followed by delithiation in the reverse scan. By lowering E_{sw} further, massive lithiation broke out with redox currents more than an order of magnitude larger and with strong hysteresis of the corresponding cathodic wave.

In contrast, the CVs obtained for the Li^+/F^- hybrid electrolytes (Fig. 7b) invariably exhibited a distinguishable anodic peak at around −1.7 V vs SHE. The dependence on E_{sw} was otherwise similar to that in the reference electrolyte, but the intense anodic peak after the massive lithiation behaved differently in the concentrated version of the Li^+/F^- hybrid electrolyte (Fig. 7b, CV series on the right). Specifically, the peak underwent significant broadening and positive shifts with increasing lithiation levels. In addition, the extensive tailing on the positive side of the peak merged with the aforementioned anodic feature characteristic of the Li^+/F^- hybrid electrolyte.

Overall, Fig. 7 suggests that the Li-activated redox reactions of Al begin with lithiation of Al by either of the following schemes:

$$Al + xLi^+ + xe^- \rightarrow AlLi_x \quad [12]$$

$$Al + xLi_2F^+ + xe^- \rightarrow AlLi_x + xLi^+ + xF^- \quad [13]$$

We favor reaction 13 rather than 12 because strongly solvated Li^+ ions are involved as the reactants in reaction 12, causing a negative balance in solvation energy. Additional support for the preference of 13 is that an appreciably stronger cathodic polarization was necessary to cause lithiation in the reference electrolytes without Li_2F^+ complexes (Fig. 7a). For simplicity, however, we do not explicitly consider the role of Li_2F^+ complexes in the following argument.

The extent to which lithiation progresses into the Al electrode depends on the time and strength of the cathodic polarization. In the Li^+/F^- hybrid electrolyte, subsequent anodic polarization can lead to fluorination and partial delithiation concomitantly.

$$AlLi_x + yF^- \rightarrow AlLi_{x-z}F_y + zLi^+ + (y+z)e^- \quad [14]$$

The resultant ternary state, $AlLi_{x-z}F_y$, would be subjected to further compositional changes by repeated redox cycling, and at some point, a steady-state reversible redox reaction may be established.

$$AlLi_{(x+a)}F_{(y-b)} + bF^- \rightleftarrows AlLi_xF_y + aLi^+ + (a+b)e^- \quad [15]$$

The anodic peak at approximately −1.7 V vs SHE in the Li^+/F^- hybrid electrolyte likely stemmed from reactions 14 or 15. These reactions probably proceeded on a solid-state basis, although we cannot totally disregard the solubility of $AlLi_xF_y$ in the solid/liquid interfacial region.

The competitive fluorination and delithiation involved in these reactions may not necessarily be concurrent but may proceed in different potential regimes, particularly when they follow massive lithiation. For example, one of the left-side CV series in Fig. 7b exhibited a strong delithiation peak separated from a relatively minor fluorination signal (red asterisks). Note, however, that the relative weight of fluorination increased in the concentrated version of the Li^+/F^- hybrid electrolyte, and the distinction between delithiation and fluorination became less apparent in the CV curves (Fig. 7b, CV series on the right). In the extreme case where fluorination dominates over delithiation (i.e., $a \sim 0$), we might alternatively view reaction 15 as reversible fluorination of Al-embedded Li.

For experimental support for reaction 15, we performed an *ex-situ* XPS depth analysis (Fig. 8) in the following manner: we performed 11 consecutive CV scans for an Al foil under a restricted

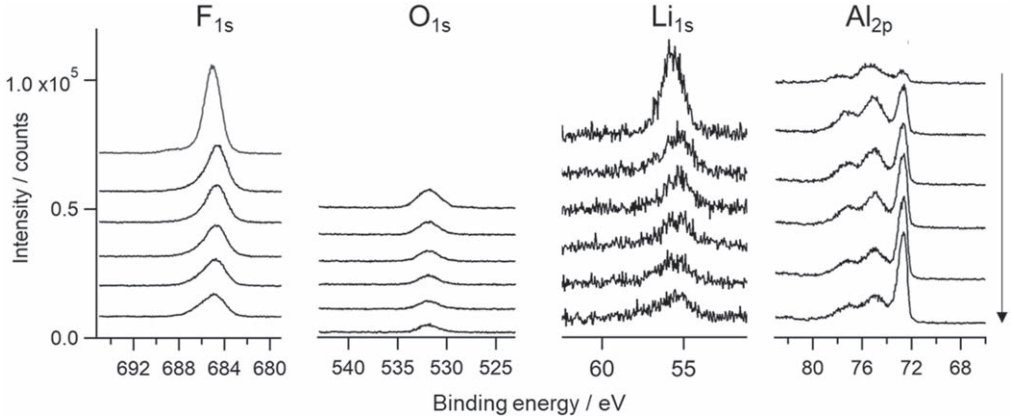

Figure 8. Series of sensitivity-corrected XPS depth-profiling spectra taken of the fluorinated state of an Al electrode subjected to 11 repeated CV scans. The spectra are aligned vertically in the increasing order of etching depth from top to bottom. The spectra were taken every 1 min of Ar^+ ion etching with the average etching depth of ∼10 nm min^{-1}.

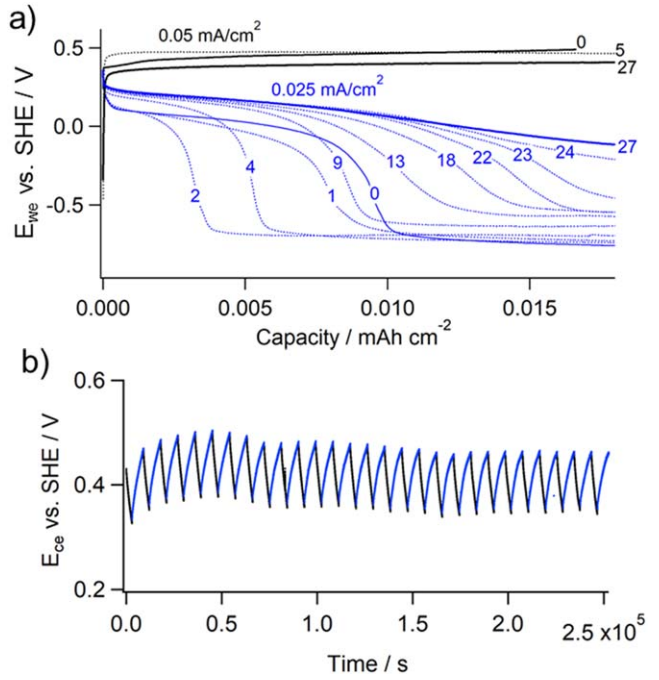

Figure 9. (a) Charge (in black) and discharge (in blue) curves measured of a Cu sheet electrode for a total of 28 cycles at moderate current densities in Li^+ (0.5 M)/F^- (38 mM) hybrid electrolyte. Cycle numbers (starting with 0) are attached to representative curves. (b) The potential vs time profile of the activated-carbon-based counter electrode during the charge/discharge cycling.

maximum cathodic polarization preventing massive lithiation. We then stopped the scan when it had just passed the anodic peak. We removed the Al electrode from the electrolyte, rinsed it with GBL, and transferred it to the XPS analysis chamber under Ar-filled airtight conditions. The Ar^+ ion etching condition was such that the depth profiling covered approximately 50 nm beneath the electrode surface. We had all the XPS signals in Fig. 8 sensitivity-corrected to directly compare them on a common intensity scale.

Figure 8 reveals the presence of a concomitant signal from residual aluminum oxides, but the results otherwise provide convincing proof that F and Li coexist as dominant elements with roughly even atomic ratios and equivalent depth distributions. Furthermore, the Al_{2p} signals, which are minor in intensity in the subsurface region, reveal high-binding-energy peaks (on the leftmost side) most likely associated with Al–F bonds. These features are consistent with the proposed Li-activated redox reaction of the Al electrode, which potentially also causes substantial electronic passivation of the electrode surface. The result of a complementary XPS depth analysis for the defluorinated (charged) state is in the Supplementary Material, Section S2. Despite some technical issues in handling the corresponding sample for *ex-situ* XPS analysis, the depth-profiling data showed at least partly the expected changes, such as a drastic intensity drop in the F_{1s} signal and the lack of the peak in the Al_{2p} signal associated with Al–F bonds.

Galvanostatic charge/discharge behaviors.—Next, we demonstrate how effectively the reversible redox reactions in the Li^+/F^- hybrid electrolytes proceeded further into the bulk of the respective metal electrode under galvanostatic conditions. We restrict the following analyses to the charge/discharge characteristics of Cu, Bi, Pb, Zn, and Al in the half-cell mode using a three-electrode beaker cell configuration.

Cu, Bi, Pb, and Zn electrodes.—Figure 9a shows the typical charge/discharge characteristics of a mechanically polished Cu sheet electrode in the Li^+(0.5 M)/F^-(38 mM) hybrid electrolyte. The

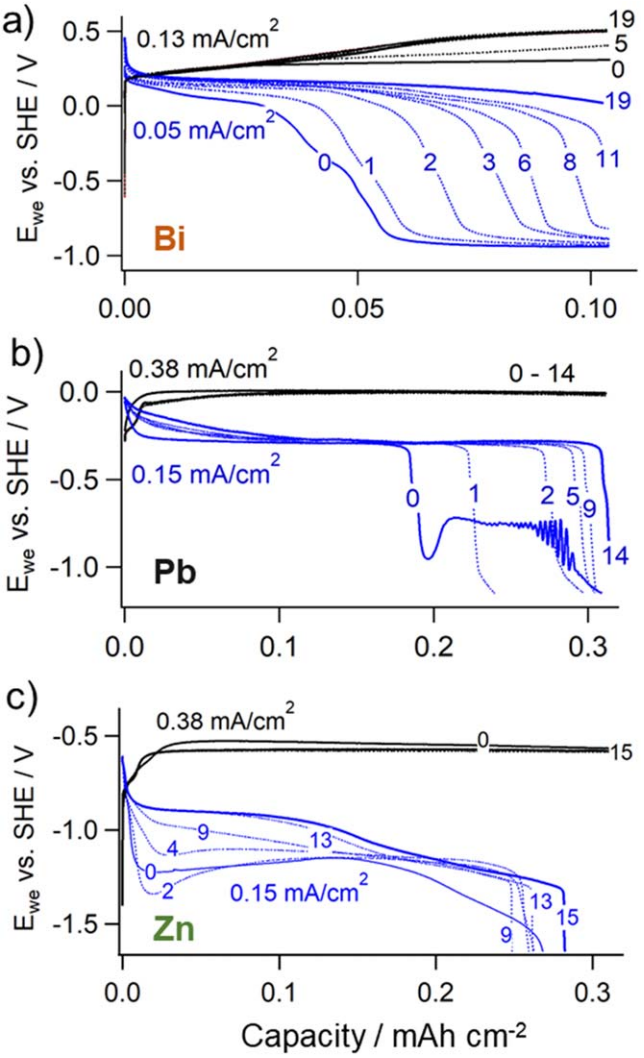

Figure 10. Cycle dependencies of charge (in black) and discharge (in blue) curves measured of (a) Bi, (b) Pb, and (c) Zn electrodes in Li^+ (0.5 M)/F^- (38 mM) hybrid electrolyte.

corresponding potential vs time profile for the activated-carbon-based counter electrode is given in Fig. 9b, illustrating the expected super-capacitor-like (sawtooth) character. We limited the charging time per cycle to 50 min and that of the discharge to 100 min under the set currents of less than 0.1 mA cm^{-2}. The necessity of a comparatively small current for charging Cu while ensuring a minor polarization may be understood from the low rate of metal-to-fluoride conversion for Cu as a transition metal with a relatively large cohesive energy.[34–36] In Fig. 9a, all the charging curves looked similar and remained almost flat for the maximum capacity of 0.018 mAh cm^{-2}. This behavior contrasts strongly with the corresponding charging of Cu in the CsF/GBL (plain fluoride-ion) electrolyte,[17] where a large polarization, exceeding 1.5 V at its maximum, accompanied the charging curve even for a limited capacity of only 0.006 mAh cm^{-2}. This severe restriction stemmed from the insoluble copper fluoride shell as an inferior ionic conductor preventing it from growing any thicker.

Thus, the flat charging curve in Fig. 9a most likely reflects the chemical dissolution of the fluoride shell in the Li^+/F^- hybrid electrolyte, which constantly re-exposes the unreacted metal surfaces to allow for smooth charging with a minor change in the electrode potential. Fluoride chemical dissolution also accounts for the distinct variation in the discharge curves by cycling, as shown in Fig. 9a. In the present system, metal deposition by discharge occurred primarily

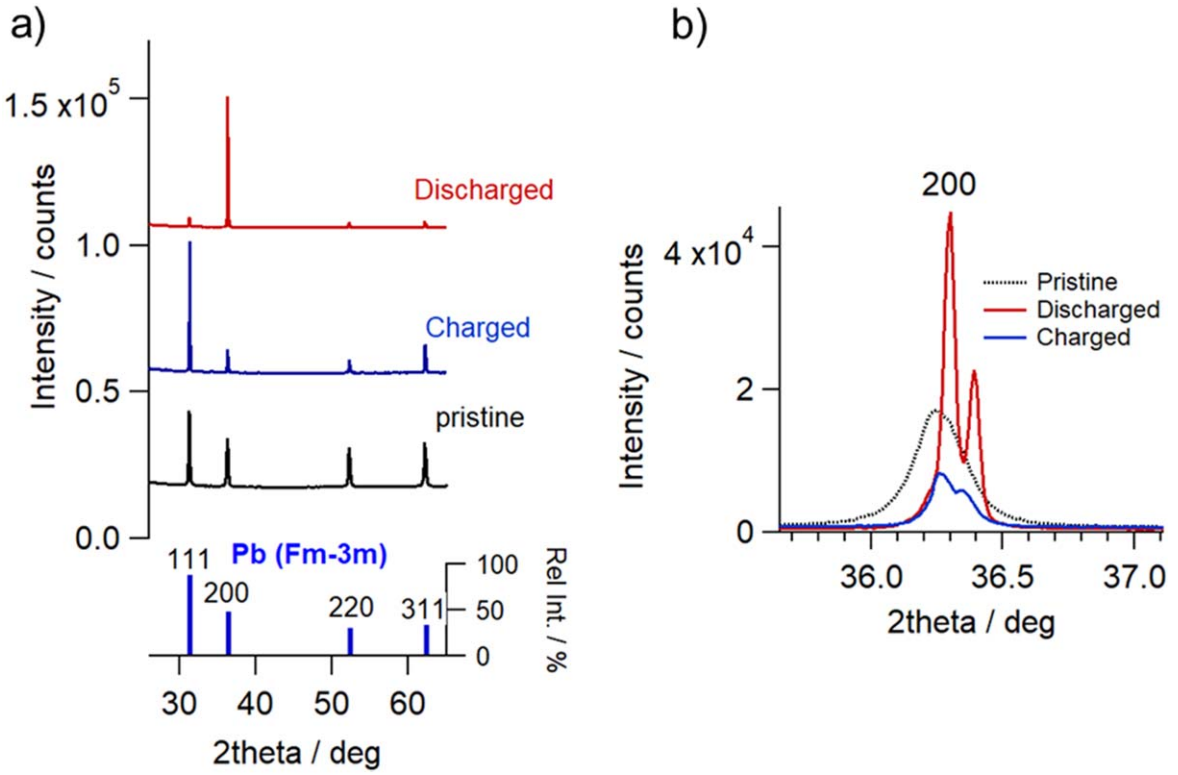

Figure 11. (a) Comparison of XRD patterns measured for a pristine Pb plate (bottom), charged state for 0.3 mAh/cm^2 (middle), and fully discharged state (top) of a Pb electrode. The lower panel shows the standard powder XRD patterns of Pb. (b) Comparison of enlarged 200 Bragg reflection signals obtained for the three different redox states.

through the reduction of dissolved metal cations. Therefore, the efficiency of the discharge process depends critically on the concentration and spatial distribution of the metal cations, which are controlled by the local solubility equilibrium in the solid/liquid interfacial region. Unless these metal cations are irreversibly lost elsewhere, the gradual shape-up of the discharge curves by cycling toward ~100% Coulombic efficiency is not surprising. In addition, the counter-electrode potential, kept within 0.4 ± 0.1 V vs SHE (Fig. 9b), assisted in minimizing metal deposition at the counter electrode.

The charge/discharge process supported by fluoride chemical dissolution represents the so-called *dissolution-and-deposition* mechanism, which results in improved cell performance rather than the more common capacity fading by cycling (see Supplementary Material, Section S3 for more detail). One needs to distinguish this mechanism from that involving electrochemical anodic metal dissolution, in which a virtually limitless amount of metal cations is released into the electrolyte, causing uncontrolled metal redeposition involving both positive and negative electrodes. Furthermore, care should be taken because the impact of fluoride chemical dissolution also depends on the cell geometry, and the mechanism operates in a more complicated manner in cells consisting of composite electrodes.

We also emphasize the fundamental roles of liquid electrolytes and the dissolution-and-deposition mechanism for FSBs, which rely on the active materials associated solely with the given pair of positive and negative electrodes. The electrolyte serves primarily as a liquid medium for fluoride shuttling to balance the metal-to-fluoride and reverse redox conversions at the two electrodes. The role of the dissolution-and-deposition mechanism is to promote these reactions that hardly proceed smoothly on a solid-state basis. The dissolved fluoride species are temporarily accumulated in the electrolyte under the local solubility equilibrium but later used for cathodic metal deposition. Regardless of the dissolution-and-deposition mechanism, the volume of the electrolyte for FSBs is preferably as small as possible for higher volumetric energy densities.

Figure 10 compares the charge/discharge curves of the Bi, Pb, and Zn electrodes in the Li^+(0.5 M)/F^-(38 mM) hybrid electrolyte. The discharge curves were likewise shaped up by cycling toward higher Coulombic efficiencies. A considerably higher charging current was allowed for these metals than for Cu, resulting in a capacity that was an order of magnitude higher for the 50 min charging period. Furthermore, the charging curve of the Bi electrode (Fig. 10a) exhibited a noticeable increase in polarization with increasing capacity. This behavior is consistent with the lowest solubility of BiF_3 in the Li^+/F^- hybrid electrolyte (cf. Fig. 2) among the metal fluorides analyzed.

Nanocrystalline fluoride structures.—Another consequence of fluoride chemical dissolution is the prohibited growth of a sufficiently thick crystalline phase of metal fluoride at the metal surface. In Fig. 10, the maximum capacities of ~0.3 mAh/cm^2 attained for the Pb and Zn electrodes correspond to a reaction depth of more than ~1 μm that underwent fluorination. Nevertheless, neither Pb nor Zn electrodes in their fluorinated states produced distinguishable XRD diffraction signals for metal fluorides. Instead, the corresponding XRD patterns manifested only metallic peaks, of which the relative intensities varied depending on the stages of charging and discharge. For example, Fig. 11a shows that the Pb electrode exhibited a marked difference in XRD patterns between the charged and discharged states. In the discharged state, the relative intensities of the four major metallic peaks varied dramatically; thus, the peak due to the 200 reflection became overwhelmingly the strongest. This tendency suggests a high degree of orientation of the metallic Pb grown by the reduction of dissolved Pb^{2+} cations. Further support for this is the enlarged 200 Bragg reflection signals (Fig. 11b), where the discharged-state metallic signal became the sharpest of all.

The FE-SEM and EDX images offer valuable complementary information regarding the charged (fluorinated) states of the metal electrodes, which gave no crystalline fluoride signals. Figure 12 shows a set of corresponding images captured for the charged

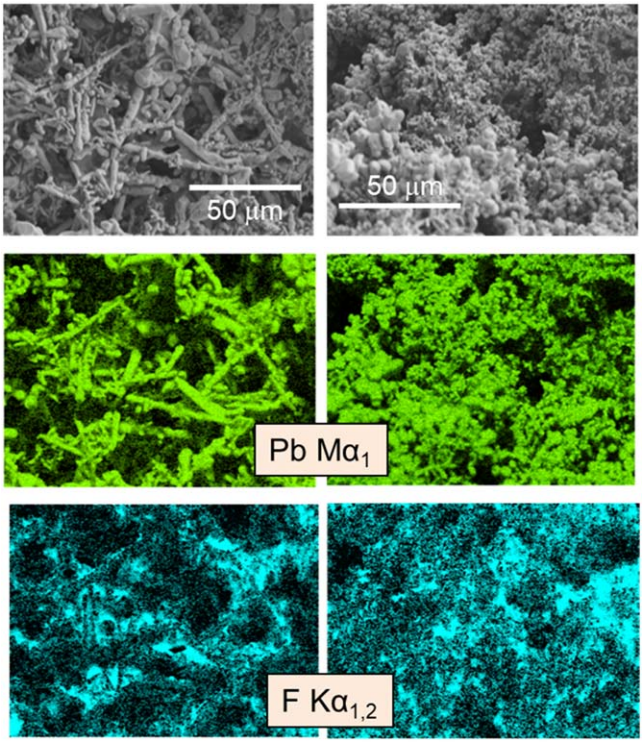

Figure 12. FE-SEM (top) and EDX (Pb and F) mapping images (middle and bottom) taken for the charged (fluorinated) state of a Pb electrode corresponding to 0.3 mAh/cm^2. Obtained for two arbitrarily selected areas near the lower edge portion of the electrode dipped in the electrolyte.

(fluorinated) state of the Pb electrode. We performed the imaging at the lower edge of the electrode portion dipped into the electrolyte, where the most significant morphologic change occurred owing to a redox-current concentration effect. The FE-SEM images show that the initial planer morphology of the Pb changed drastically to a fine granular structure. The EDX mapping based on the distribution of the Pb Mα_1 signal corresponded well with the SEM image, whereas those based on the F K$\alpha_{1,2}$ did not, as expected. Nevertheless, the position-averaged F/Pb elemental ratio in these images was as large as 1.4: 1, which corroborates the presence of a significant amount of lead fluorides (if not in crystalline form) wherever on the Pb electrode in the charged state.

The comparative series of FE-SEM and EDX images obtained for the discharged state of the Pb electrode (Fig. 13) proved a reversible defluorination by the discharge. Namely, the F K$\alpha_{1,2}$ EDX image became dark, and the position-averaged F/Pb ratio dropped below ~10%. Furthermore, the FE-SEM image in Fig. 13 reveals faceted Pb crystallites, which account for the overwhelmingly strong and sharp 200 Bragg reflection signals observed in Fig. 11b.

Al electrode.—We also investigated the unique, Li-activated redox reactions of Al in the framework of galvanostatic charge/discharge measurement. We favored the concentrated version of the Li^+/F^- hybrid electrolyte with the highest possible concentration (0.15 M) of F^- ions (as Li_2F^+ complexes) and excess Li^+ ions at ~1 M. This is because Li^+ ions (more importantly Li_2F^+ complexes; see reactions 12 and 13)) are prerequisites for the formation of the ternary state ($AlLi_xF_y$), and the higher the concentration of fluoride species, the easier the Li-activated fluorination (cf. Fig. 7).

Figure 14 shows the typical charge/discharge cycle behavior of polished Al foil at a comparatively high redox current of 0.38 mA cm^{-2}. The flat charging curves were almost invariant by cycling. The discharge curves exhibited more expansive plateaus upon cycling and became stationary for 16–40 cycles with no capacity fading. Furthermore, the steady-state Coulombic efficiency commonly exceeded 95%. We calculated the specific capacity in Fig. 14 per total weight of a 20 μm-thick Al foil dipped into the electrolyte; therefore, the maximum capacity of ~100 mAh g^{-1} gained in Fig. 14 is not a trivial value. We could further increase the capacity at least two- or three-fold while preserving superior cyclability.

The highly reversible and high-capacity charge/discharge demonstrated in Fig. 14 is distinctive from the standard electrochemical lithiation/delithiation processes of Al.[30–33] A comparative study using the same Al-foil electrode but in a reference electrolyte consisting of only LiFSI (1 M) showed that charge/discharge progressed under noticeably more negative redox potentials, yielding the maximum Coulombic efficiency below ~90% with unavoidable capacity fading (Supplementary Material, Section S4). Furthermore, the extended lithiation/delithiation cycling led to an increasingly fragile Al electrode structure, eventually breaking apart in the electrolyte.

Figure 15 compares *ex-situ* XRD patterns obtained for a pristine Al foil (top) and the fully charged (middle) or discharged (bottom) state corresponding to the right ends of the charge/discharge curves in Fig. 14. In the survey profiles (left side), Al 111 and 200 reflections seemed still dominant for both charged and discharged states. The minor signals at 40.2° came from 312 or 420 reflections attributed to a β-LiAl phase.[37] Their intensities did not vary significantly between the charged and discharged state. This fact suggests that the principal redox reactions behind the charge/discharge curves in Fig. 14 are not the common lithiation and delithiation processes (cf. Supplementary Material, Fig. S7b).

Furthermore, the enlarged Al 220 signals in Fig. 15 (right side) demonstrate considerable deformation in the peak shapes both in charged and discharged states. We observed analogous deformations for all other major Al peaks. More specifically, the 220 signal of the pristine Al foil consisted of a clear Cu K$_{\alpha1}$ and Cu K$_{\alpha2}$ doublet with a 2:1 intensity ratio. However, the signals for the charged and discharged states violated this standard ratio and resembled a triplet. This deformation strongly suggests that the observed signal could be a superposition of the adjacent Al 220 and LiF 220 reflections.[38] The proposed Li-activated redox reaction, reaction 14, or equivalently the fluorination of Al-embedded Li, seems to justify the formation of such LiF-like intermediate phases with mixed Al–Al and Li–F bonds.

It should also be emphasized that the reversible and cyclable Al-based negative electrodes with minor polarization, when combined with Bi- or Cu-based positive electrodes, hold significant potential for application in high-voltage (2–3 V class) FSB cells. Moreover, the Li-activated redox reactions of Al discussed above enable a thin Al sheet or foil to serve simultaneously as an active material and a current collector. Thus, we no longer need a composite form made partly of a conductive assistant, such as AB, for Li-activated Al electrodes. This advantage can also aid in preventing the drawbacks associated with such carbon-based addenda, which often promote reductive decompositions of the electrolyte in the high-negative potential region.

Charge/discharge behaviors of composite electrodes.—Unlike the Al negative electrode, for positive electrode materials, such as those based on Bi/BiF_3 and Cu/CuF_2 redox conversions, composite electrodes are essential to gain practically acceptable half-cell capacities. The behavior of such composite electrodes, especially those made of BiF_3 (CuF_2) nano-composites, is qualitatively different from that of plain metal electrodes (Supplementary Material, Section S5). The conductive assistant (typically AB) plays a critical role as the exclusive path of electrons for redox reactions in the case of composite electrodes. The surfaces of the conductive AB chains also serve as preferential sites for the reduction of metal cations in the electrolyte according to the dissolution-and-deposition mechanism. The compatibility of the Li^+/F^- hybrid electrolyte with such composite electrodes and stable full-cell operations in combination with the Li-activated Al electrode will be detailed elsewhere in a separate article (see Supplementary Material, Section S5 for a brief account).

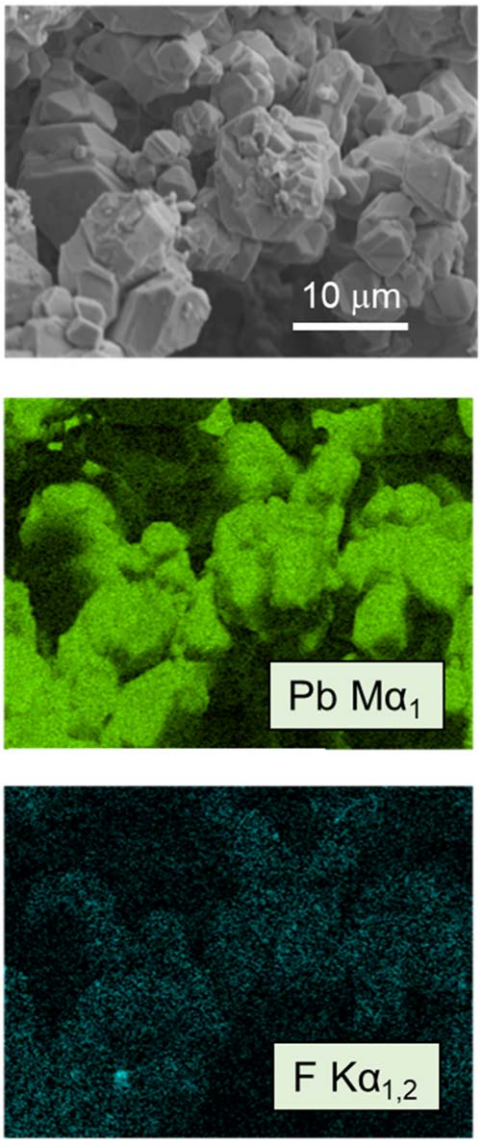

Figure 13. FE-SEM (top) and EDX (Pb and F) mapping images (middle and bottom) taken for the discharged (defluorinated) state of a Pb electrode corresponding to a specific capacity of 0.3 mAh/cm^2. The FE-SEM image revealed faceted Pb crystallites accounting for the strong 200 Bragg reflection signal dominating the corresponding XRD pattern in Fig. 11. The dark F Kα EDX image (bottom) is characteristic of the defluorinated state with a position-averaged F/Pb elemental ratio of less than 10%.

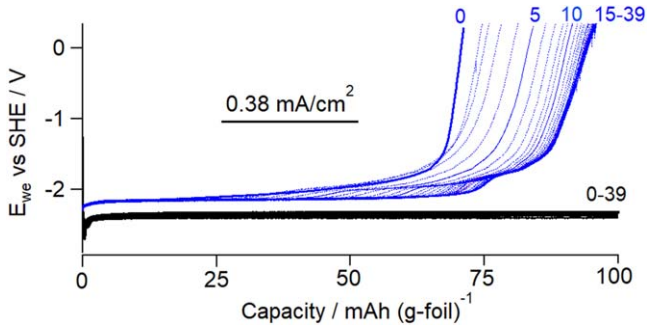

Figure 14. A collection of typical charge (in black) and discharge (in blue) curves of an Al foil (20 μm thick) in the concentrated version of Li^+/F^- hybrid electrolyte measured for a total of 40 repeated cycles. The specific capacity (horizontal axis) refers to the total weight of the Al electrode brought into the electrolyte.

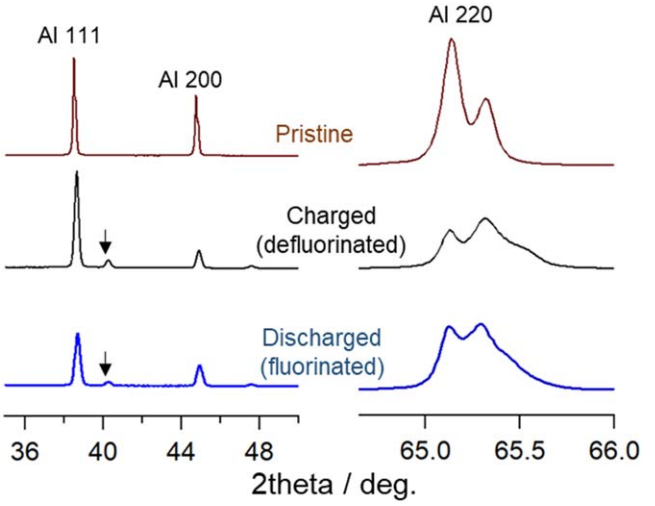

Figure 15. Comparison of *ex-situ* XRD patterns of pristine Al foil (top) and of its charged (middle) and discharged (bottom) states derived after the extensive charge and discharge cycling of Fig. 14. The minor diffraction peaks at 2θ/deg = 40.2 (indicated by short arrows) represent the residual AlLi alloy phase.

The behaviors of the composite electrodes also give us hints for the future direction of FSBs using the Li^+/F^- hybrid electrolytes. The currently available maximum fluoride concentration in the concentrated version is 0.15 M in combination with 1 M Li^+. This higher fluoride concentration was more advantageous, especially for the composite electrodes with large specific surface areas of the active materials contacting the electrolyte, thereby enabling significantly high charge-discharge rates (Fig. S9). The effective fluoride concentration may be increased further by increasing the Li^+ concentration to above 1 M to aid the Li_2F^+ complex formation. However, the solubility of the Li salts in GBL is upper limited to $\sim$2 M, and a probable increase in viscosity accompanying such high ionic strengths might negatively affect the electrolyte performance. Under this limitation, it seems more fruitful to aim for better structural, compositional, and electrochemical optimizations of the active and other supporting materials for the composite electrodes towards high-energy-density FSBs working with the dissolution-and-deposition mechanism enabled by the hybrid electrolytes.

Summary and Conclusion

High-boiling, organic, liquid-based FSBs can solve many critical issues facing the metal-to-fluoride and reverse redox conversions essential for FSBs. The resultant significant volume changes of the active materials are not severe problems in the liquid-based systems if the metal fluoride phase in the redox conversions allows for controllable solubilization in the given liquid electrolyte. "Controllable" implies avoiding excessive fluoride dissolution, which causes a significant fraction of the dissolved ions to be irreversibly lost. The overall process assisted by fluoride chemical dissolution referred to as the *dissolution-and-deposition* mechanism is equivalent to the redox conversion between the metal and metal fluorides and is compatible with fluorides that are poor electronic and ionic conductors. This concept is key to the reversible operation of positive electrodes.

Liquid-based FSBs must also satisfy several fundamental criteria. They must possess fluoride ions at the minimum required concentration and require AAs to control the chemical and electrochemical activities of fluoride ions, preventing them from promoting irreversible subreactions of organic solvents. However, AAs must bind fluoride ions relatively loosely so that AA–F^- complexes can liberate fluoride ions near the electrode/liquid interface where the metal/fluoride conversions progress. In addition, AAs themselves must possess sufficient redox stability on their own.

The lactone-based $Li^+/F^-(Mg^{2+}/F^-)$ hybrid electrolytes developed in the present work can meet these critical requirements for the liquid electrolyte for FSBs. The binding of F^- by Li^+ and Mg^{2+} to yield soluble Li_2F^+ and MgF^+ complexes means that Li^+ and Mg^{2+} act as inorganic AAs that are hardly reduced nor oxidized in the whole potential range for which we operate FSBs. The Li_2F^+ and MgF^+ complexes do not bind F^- anions too strongly and can thus serve as the effective sources of the fluoride ions for the metal-to-fluoride redox conversion at the electrode/liquid interface. This ability is appreciably higher for the Li_2F^+ complex that bound F^- anions more loosely than the MgF^+ complex. The concentrated versions of the $Li^+/F^-(Mg^{2+}/F^-)$ hybrid electrolytes ensured that these complexes were present at a concentration of ~0.15 M with excess $Li^+(Mg^{2+})$ and FSI^- ($TFSI^-$) ions. Furthermore, we found that the Li_2F^+ and MgF^+ complexes catalytically promoted the chemical dissolution of metal fluorides in the relatively positive redox series, including ZnF_2, PbF_2, BiF_3, and CuF_2, to the extent that the dissolution-and-deposition mechanism worked in an almost ideal manner.

The Li^+/F^- hybrid electrolyte, in combination with an Al electrode, broke the trend of negative-electrode materials being incompatible with the dissolution-and-deposition mechanism. In the Li^+/F^- hybrid electrolyte, the lithiation of the Al electrode gave rise to a Li-activated fluorination path as a highly competitive anodic process. After repeated charge/discharge pre-cycling, the electrode attained $AlLi_xF_y$ ternary compositions over depths of the order of ~10 μm and underwent reversible fluorination/defluorination with 95%–100% Coulombic efficiencies. The specific capacity gained by this reaction is sufficient for combination with appropriate positive electrodes to build up high-voltage FSB cells.

In conclusion, we have demonstrated what the previously reported FSB-oriented liquid electrolytes could not achieve by developing the $Li^+/F^-(Mg^{2+}/F^-)$ hybrid electrolytes. The key is using Li^+ and Mg^{2+} ions as inorganic AAs with ultimate redox stability. The Li^+/F hybrid electrolyte also enabled a unique Li-activated redox conversion of an Al electrode.

Acknowledgments

This work is based on results obtained from projects, JPNP16001 and JPNP21006, commissioned by the New Energy and Industrial Technology Development Organization (NEDO). The authors gratefully acknowledge Ms. Yumiko Kikumoto for her extensive technical support throughout the present work. We thank Mr. Hideo Nishihara for his assistance with the experiments.

ORCID

Mitsuo Kawasaki https://orcid.org/0000-0002-4642-5755
Yuko Yokoyama https://orcid.org/0000-0002-3943-0978

References

1. M. A. Reddy and M. Fichtner, *J. Mater. Chem.*, **21**, 17059 (2011).
2. F. Gschwind, G. Rodriguez-Garcia, D. J. S. Sandbeck, A. Gross, M. Weil, M. Fichtner, and N. Hörmann, *J. Fluorine Chem.*, **182**, 76 (2016).
3. G. Karkera, M. A. Reddy, and M. Fichtner, *J. Power Sources*, **481**, 228877 (2021).
4. K. Okazaki, Y. Uchimoto, T. Abe, and Z. Ogumi, *ACS Energy Lett.*, **2**, 1460 (2017).
5. V. K. Davis et al., *Science*, **362**, 1144 (2018).
6. A. C. Cope, N. A. LeBel, P. T. Moore, and W. R. Moore, *J. Am. Chem. Soc.*, **83**, 3861 (1961).
7. H. Konishi, T. Minato, T. Abe, and Z. Ogumi, *Chem. Lett.*, **47**, 1346 (2018).
8. H. Konishi, R. Takekawa, T. Minato, Z. Ogumi, and T. Abe, *Chem. Phys. Lett.*, **755**, 137785 (2020).
9. H. Konishi, T. Minato, T. Abe, and Z. Ogumi, *J. Electroanal. Chem.*, **871**, 114103 (2020).
10. A. C. Kucuk, T. Minato, T. Yamanaka, and T. Abe, *J. Mater. Chem. A, 2019*, **7**, 8559 (2019).
11. A. C. Kucuk, T. Yamanaka, and T. Abe, *Solid State Ionics*, **357**, 115499 (2020).
12. A. C. Kucuk and T. Abe, *J. Florine Chem.*, **240**, 109672 (2020).
13. A. C. Kucuk and T. Abe, *J. Power Sources*, **496**, 229828 (2021).
14. A. C. Kucuk, T. Yamanaka, and T. Abe, *J. Mater. Chem. A*, **8**, 22134 (2020).
15. T. Yamamoto, K. Matsumoto, R. Hagiwara, and T. Nohira, *ACS Appl. Energy Mater.*, **2**, 6153 (2019).
16. T. Yamamoto, K. Matsumoto, R. Hagiwara, and T. Nohira, *J. Electrochem. Soc.*, **168**, 040530 (2021).
17. M. Kawasaki, K. Morigaki, G. Kano, H. Nakamoto, R. Takekawa, J. Kawamura, T. Minato, T. Abe, and Z. Ogumi, *J. Electrochem. Soc.*, **168**, 010529 (2021).
18. R. E. Connick and M.-S. Tsao, *J. Am. Chem. Soc.*, **76**, 5311 (1954).
19. Y. Fovet and J.-Y. Gal, *Talanta*, **53**, 617 (2000).
20. N. Shibata, H. Sato, S. Sakaki, and Y. Sugita, *J. Phys. Chem. B*, **115**, 10553 (2011).
21. M. Kawasaki, H. Kiuchi, K. Shimoda, G. Kano, H. Fujimoto, Z. Ogumi, and T. Abe, *J. Electrochem. Soc.*, **167**, 120518 (2020).
22. N. Mozhzhukhina and E. J. Calvo, *J. Electrochem. Soc.*, **164**, A2295 (2017).
23. T. Pilz, T. Schleid, and M. Jansen, *Z. Anorg. Allg. Chem.*, **639**, 2555 (2013).
24. I. G. Shenderovich, S. N. Smirnov, G. S. Denisov, V. A. Gindin, N. S. Golubev, A. Dunger, R. Reibke, S. Kirpekar, O. L. Malkina, and H.-H. Limbach, *Ber. Bunsenges. Phys. Chem.*, **102**, 422 (1998).
25. A. Sadoc, M. Body, C. Legein, M. Biswal, F. Fayon, X. Rocquefelte, and F. Boucher, *Phys. Chem. Chem. Phys.*, **13**, 18539 (2011).
26. M. Yamawaki, M. Hirai, M. Yasumoto, and M. Kanno, *J. Nucl. Sci. Tech.*, **19**, 563 (1982).
27. H. Kato, J. Niwa, and K. Hirao, *Nippon Kagaku Kaishi*, **1984**, 1055 (1984).
28. F. A. Fernandez-Lima, O. P. VilelaNeto, A. S. Pimentel, C. R. Ponciano, M. A. C. Pacheco, M. A. Chaer Nascimento, and E. F. da Silveira, *J. Phys. Chem. A*, **113**, 1813 (2009).
29. E. Rehm, A. I. Boldyrev, and P. V. R. Schleyer, *Inorg. Chem.*, **31**, 4834 (1992).
30. S. Z. E. Abedin, A. Garsuch, and F. Endres, *Aust. J. Chem.*, **65**, 1529 (2012).
31. F. Zhang, B. Ji, X. Tong, M. Sheng, X. Zhang, C.-S. Lee, and Y. Tang, *Adv. Mater. Interfaces*, **3**, 1600605 (2016).
32. M. Z. Ghavidel, M. R. Kupsta, J. Le, E. Feygin, A. Espitia, and M. D. Fleischauer, *J. Electrochem. Soc.*, **166**, A4034 (2019).
33. B. Qin, T. Diemant, H. Zhang, A. Hoefling, R. J. Behm, J. Tübke, A. Varzi, and S. Passerini, *ChemSusChem*, **12**, 2609 (2019).
34. K. Kambe, *Phys. Rev.*, **99**, 419 (1955).
35. *CRC Handbook of Chemistry and Physics* (CRC Press, Boca Raton, FL) 75th ed. ed., 6, p.110 (1994).
36. M. A. Turchanin and P. G. Agraval, *Powder Metall. Met. Ceram.*, **47**, 26 (2008).
37. T. O. Brun, S. Susman, R. Dejus, B. Granéli, and K. Sköld, *Sold. State. Commu.*, **45**, 721 (1983).
38. J. Yamashita and S. Asano, *J. Phys. Soc. Jpn.*, **52**, 3506 (1983).